Engineering stable electrocatalysts by synergistic stabilization between carbide cores and Pt shells

nature materials

LETTERS

https://doi.org/10.1038/s41563-019-0555-5

Engineering stable electrocatalysts by synergistic stabilization between carbide cores and Pt shells

Daniel Göhl[1,2,7], Aaron Garg[3,7], Paul Paciok[4], Karl J. J. Mayrhofer[1,5], Marc Heggen[4], Yang Shao-Horn[6], Rafal E. Dunin-Borkowski[4], Yuriy Román-Leshkov[3*] and Marc Ledendecker[1*]

Core–shell particles with earth-abundant cores represent an effective design strategy for improving the performance of noble metal catalysts, while simultaneously reducing the content of expensive noble metals[1–4]. However, the structural and catalytic stabilities of these materials often suffer during the harsh conditions encountered in important reactions, such as the oxygen reduction reaction (ORR)[3–5]. Here, we demonstrate that atomically thin Pt shells stabilize titanium tungsten carbide cores, even at highly oxidizing potentials. In situ, time-resolved experiments showed how the Pt coating protects the normally labile core against oxidation and dissolution, and detailed microscopy studies revealed the dynamics of partially and fully coated core–shell nanoparticles during potential cycling. Particles with complete Pt coverage precisely maintained their core–shell structure and atomic composition during accelerated electrochemical ageing studies consisting of over 10,000 potential cycles. The exceptional durability of fully coated materials highlights the potential of core–shell architectures using earth-abundant transition metal carbide (TMC) and nitride (TMN) cores for future catalytic applications.

The development of core–shell nanostructures with controllable size, shell thickness, surface facets and composition vastly expands the possibility for engineering noble metal catalysts with enhanced performance[4]. Numerous core–shell systems have been synthesized for catalytic applications, very often with other noble metal cores, such as Ru (refs. [6,7]), Pd (refs. [5,8]), Ag (ref. [9]) and Ir (ref. [10]) with marginal cost benefits. Critically, these core–shell materials along with those comprising earth-abundant, metallic cores (for example, Fe, Co and Ni) form intrinsically metastable structures with miscible core and shell elements that degenerate during electrochemical cycling or annealing due to metal leaching or migration[5,7,8,11]. These instabilities result in considerable losses in active surface area and performance over time, imposing major barriers for the broad usage of core–shell architectures in industrial applications, where stability is essential. This is especially true for fuel cell technologies, the commercialization of which has been hindered by the poor durability of ORR catalysts[3,12–14].

Early TMCs and TMNs are ideal core materials due to their thermal and chemical stability, electrical conductivity, low cost and intrinsic ability to bind strongly to noble metals while still being immiscible with them[15,16]. Unfortunately, the formation of surface oxides or carbon on TMCs and TMNs presents a difficult synthetic challenge for the deposition of atomically thin, uniform noble metal shells[15,17]. As a result, only a few examples of core–shell systems comprising noble metal shells and TMC or TMN cores have been reported[18,19]. Recently, we demonstrated a versatile synthetic method that circumvents these challenges via a high temperature self-assembly allowing for the synthesis of Pt shells on titanium tungsten carbide (Pt/TiWC) and titanium tungsten nitride (Pt/TiWN) cores with controllable shell coverage[15,20,21]. These core–shell materials display unique catalytic properties resulting from bonding interactions between the shell and the core, including weakened adsorbate binding and extremely high sinter-resistance, but their durability in electrochemical environments has received only minor attention so far.

Here, we conducted a detailed examination of the electrochemical stability of Pt/TiWC and Pt/TiWN nanoparticles (NPs) as a function of two different Pt coverages to help identify possible underlying degradation mechanisms. Specifically, a scanning flow cell with inductively coupled plasma–mass spectrometry (SFC–ICP–MS) was used to measure metal dissolution as a function of potential, and identical location–scanning transmission electron microscopy (IL–STEM) paired with energy dispersive X-ray spectroscopy (EDX) was used to track changes to the structure of individual particles. In addition to possessing exemplary structural stability, fully coated core–shell materials demonstrated durability as ORR catalysts. Together, these results provide important insights on the design of stable core–shell catalysts with earth-abundant elements.

To determine the effect of the Pt shell coverage on the electrochemical stability, we synthesized nominal 0.7 monolayer (ML) Pt/TiWC and 2 ML Pt/TiWC using methods previously reported by our group[15,20]. The carbon-supported materials (around 20 wt% core–shell particles, Ti/W ratio around 10/90) were characterized by transmission electron microscopy (TEM) (Supplementary Fig. 1) to determine particle size distributions and ICP–MS (Supplementary Table 1) to determine elemental compositions. The particle size distributions for 0.7 ML Pt/TiWC and 2 ML Pt/TiWC were 5.1 ± 1.3 nm and 6.6 ± 1.8 nm, respectively. The average Pt shell thickness was then estimated from the average particle size and the elemental composition.

As a first indication of stability, the dissolution of carbide-based core–shell particle elements was examined in situ via SFC–ICP–MS. To establish a clear relationship between the applied potential and

[1]Department of Interface Chemistry and Surface Engineering, Max-Planck-Institut für Eisenforschung, Düsseldorf, Germany. [2]Faculty of Chemistry and Biochemistry, Ruhr-Universität Bochum, Bochum, Germany. [3]Department of Chemical Engineering, Massachusetts Institute of Technology, Cambridge, MA, USA. [4]Ernst Ruska-Centre for Microscopy and Spectroscopy with Electrons and Peter Grünberg Institute, Forschungszentrum Jülich GmbH, Jülich, Germany. [5]Helmholtz Institute Erlangen-Nürnberg for Renewable Energy, Forschungszentrum Jülich GmbH, Erlangen, Germany. [6]Department of Mechanical Engineering and Department of Materials Science and Engineering, Massachusetts Institute of Technology, Cambridge, MA, USA. [7]These authors contributed equally: Daniel Göhl, Aaron Garg. *e-mail: yroman@mit.edu; m.ledendecker@mpie.de

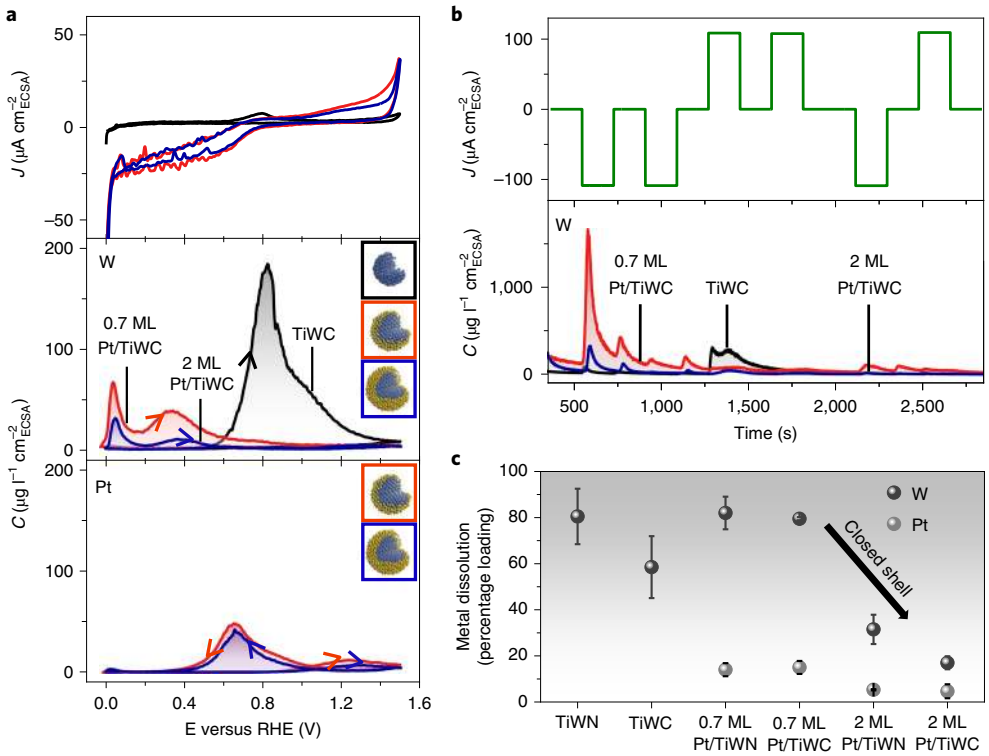

Fig. 1 | SFC–ICP–MS single potential cycle and galvanostatic measurements. a, First CV at 2 mV s^{-1} between 0.0 and 1.5 V_{RHE} (upper panel) in 0.1 M $HClO_4$ (dilute O_2, see Methods) and the corresponding dissolution concentration (C) profiles of W (middle panel) and Pt (lower panel) as a function of potential (E). **b**, Applied current density (J) profile in 0.1 M $HClO_4$ (dilute O_2) during the galvanostatic measurements and the corresponding dissolution profile of W with time. **c**, Total amount of metal dissolution during the galvanostatic measurements. Error bars represent s.d. of at least three independent measurements.

metal dissolution, a slow cyclic voltammetry (CV) scan was conducted at 2 mV s^{-1} from 0.0 to 1.5 V_{RHE} (reversible hydrogen electrode) in 0.1 M $HClO_4$ on the core–shell NPs as well as on bare TiWC NPs supported on carbon (Fig. 1a)[22]. For the Pt-containing samples, oxidation of Pt occurs around 1.0 V_{RHE} and is accompanied by slight dissolution up to 1.5 V_{RHE}, but most Pt dissolution occurs during the cathodic scan when the formed Pt oxides are reduced to Pt^0 near 0.7 V_{RHE}, as previously shown by Topalov et al.[23]. For bare face centred cubic TiWC NPs, the CV scan showed oxidation beginning at roughly 0.6 V_{RHE}, coinciding directly with severe W dissolution (Ti dissolution profile in Supplementary Fig. 2). Previous studies on bulk hexagonal WC showed similar behaviour, although at slightly higher potentials being the thermodynamically more stable phase[24,25].

The Pt/TiWC core–shell materials displayed a markedly different W dissolution profile compared to the bare carbide. In contrast to the single oxidative W dissolution peak for TiWC, Pt/TiWC showed two smaller dissolution peaks at lower potentials. The first peak at 0.05 V_{RHE} can be attributed to the Pt-catalysed reduction of remaining surface WO_3 from passivation, while the second peak at 0.35 V_{RHE} corresponds to re-oxidation and subsequent dissolution of these reduced surface oxides. This effect is supported by SFC–ICP–MS experiments on Pt NPs deposited onto bulk WC, where the same two peaks were observed in the first scan from 0.0 to 0.5 V_{RHE} but disappeared in later cycles (Supplementary Fig. 3). These peaks only reappeared after severe oxidation of WC while cycling up to 1.5 V_{RHE}, thus strongly indicating that the dissolution peaks below 0.5 V_{RHE} are related to the initial state of the surface oxides, rather than to dissolution of WC from the bulk. From thermodynamics, the initial W dissolution occurs in the potential range corresponding to a transition from WO_3 to lower W oxides[26], yet similar experiments on bulk WO_3 showed much less dissolution at these potentials[24]. Since these peaks appear more noticeably in the presence of Pt, it is likely that Pt catalyses the reduction of surface WO_3, leading to the observed dissolution at low potentials. Notably, almost no W dissolution was observed for the Pt/TiWC samples above 0.6 V_{RHE} where bare TiWC dissolved severely. This difference is strong evidence that the Pt shell protects the carbide core from dissolution at these elevated potentials, and no further W dissolution was measured during the cathodic scan or the second cycle (Supplementary Fig. 4).

To obtain a more extensive overview of the stability performance, harsh galvanostatic measurements were performed with the SFC–ICP–MS switching between constant oxidative and reductive current densities of 0.1 mA cm^{-2}_{ECSA}. Potentials ranged from −0.5 V_{RHE} under reductive currents up to 2.0 V_{RHE} under oxidative currents, depending on the sample (Supplementary Fig. 5). The dissolution profiles for the galvanostatic measurements revealed the same general features as in the single CV experiments for all the samples, namely dissolution during reduction of surface oxides and during oxidation of unprotected TiWC (Fig. 1b). However, integration of the dissolved elements over the whole galvanostatic sequence indicated that the sample with sub-ML Pt coverage experienced almost complete core dissolution under these aggressive conditions, while the thicker Pt shell was able to substantially suppress dissolution of the carbide core (Fig. 1c). The synthesis was extended to TiWN cores with 0.7 and 2 ML Pt shells, which showed the same stabilizing trend with increased shell coverage (Supplementary Fig. 5b). At potentials surpassing 1.9 V_{RHE}, much higher than the potentials at which bare TiWC and TiWN NPs undergo oxidative dissolution, only 17 and 31% of W dissolved for 2 ML Pt/TiWC and 2 ML Pt/TiWN, respectively. In comparison, roughly 80% of W dissolved for both 0.7 ML Pt/TiWC and 0.7 ML Pt/TiWN, demonstrating the critical importance of the Pt shell coverage and thickness for

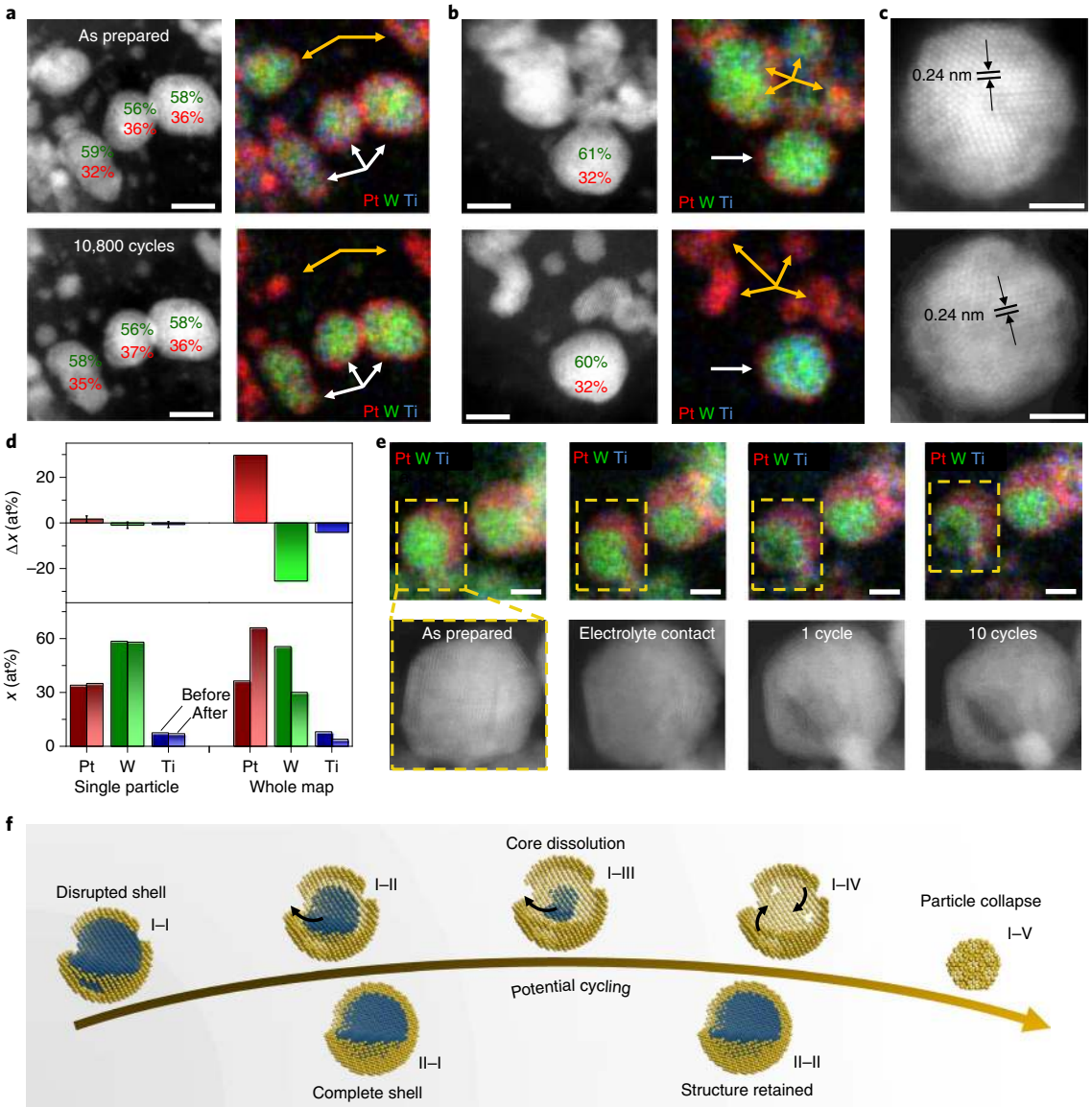

Fig. 2 | Structural stability during potential cycling. a–c, Identical location STEM images and corresponding EDX elemental maps (IL-STEM-EDX) of 2 ML Pt/TiWC before (upper panel) and after (lower panel) ASTs showing particles with complete (white arrows) and incomplete (orange arrows) Pt shells. The AST consisted of 10,800 cycles between 0.4 and 1.0 V_{RHE} in Ar-sat 0.1 M $HClO_4$ at a scan rate of 1 V s^{-1}. Scale bars, 5 nm (**a**), 4 nm (**b**) and 2 nm (**c**). **d**, Change in elemental composition (x) measured by EDX of individual particles with complete Pt shells and the whole map after the AST. **e**, IL-STEM-EDX of 2 ML Pt/TiWC as prepared, after electrolyte contact, after one cycle and after ten cycles in 0.1 M $HClO_4$. Scale bars, 4 nm. **f**, Schematic showing the evolution of partially and fully coated core–shell particles during potential cycling.

protecting the core from dissolution and therefore on the overall stability of the core–shell particles. The sub-ML Pt samples displayed even more dissolution than bare TiWC and TiWN NPs, particularly for Ti (Supplementary Fig. 5c). We suggest that Pt may accelerate the dissolution of exposed core surfaces at the interface through Pt-catalysed reduction or oxidation, further emphasizing the importance of complete, uniform shell coverage.

In addition to the dissolution behaviour, we followed the structural and compositional evolution of individual 2 ML Pt/TiWC NPs before and after an accelerated stress test (AST) with IL–STEM–EDX. The AST was conducted in Ar-sat 0.1 M $HClO_4$ with 10,800 cycles between 0.4 and 1.0 V_{RHE} at a scan rate of 1 V s^{-1}. As shown in Fig. 2 and Supplementary Fig. 6, particles with uniform Pt shells demonstrated remarkable stability, maintaining their core–shell structure over thousands of potential cycles without leaching or forming an alloy with Pt. These particles also did not agglomerate or coalesce as is typical of Pt/C NPs, which is consistent with previously reported evidence for the extremely high sinter-resistance of Pt/TiWC stemming from the strong bonding between the shell and the core elements[15,20]. High-resolution STEM revealed that the carbide crystal lattice remained unchanged with an interplanar distance of 0.24 nm corresponding to face centred cubic WC(111) planes (Fig. 2c). Furthermore, the amounts of Pt, W and Ti changed negligibly for these particles, indicating that the atomic composition was also conserved (Fig. 2d). These unique findings suggest a synergistic stabilizing effect in which the Pt shell protects the labile core from dissolution, while the TiWC core binds strongly to the Pt shell, anchoring it in place and preventing agglomeration. In contrast, particles that did not have complete Pt coverage showed dissolution of the TiWC core and collapsed to form ~4–5 nm Pt NPs (Fig. 2a,b). Additional IL–STEM measurements monitored the degradation of partially coated 2 ML Pt/TiWC in the first ten cycles (Fig. 2e

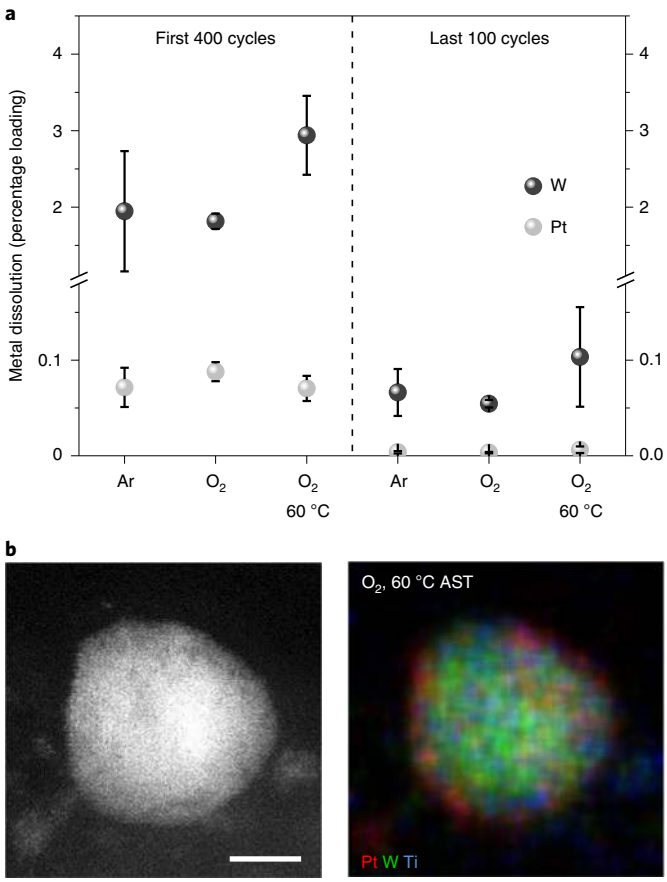

Fig. 3 | Long-term durability in O_2-sat electrolyte and at elevated temperature. a, Total amount of W and Pt dissolution measured via SFC–ICP–MS for 2 ML Pt/TiWC during the first 400 and last 100 cycles of an AST consisting of 1,000 cycles from 0.4 to 1.0 V_{RHE} at 1 V s^{-1} in Ar or O_2-sat 0.1 M $HClO_4$ at room temperature or 60 °C. Error bars represent s.d. of at least three independent measurements. **b**, STEM image and corresponding EDX elemental map of a 2 ML Pt/TiWC NP after 10,800 cycles from 0.4 to 1.0 V_{RHE} at 1 V s^{-1} in O_2-sat 0.1 M $HClO_4$ at 60 °C. Scale bar, 3 nm.

and Supplementary Fig. 7). While slight dissolution of exposed core species was observed after electrolyte contact, most dissolution and restructuring took place during the first cycle, followed by less change between cycles one and ten. Particles with greater core exposure dissolved more rapidly, confirming the influence of Pt coverage on the rate of core dissolution (Supplementary Fig. 7).

To evaluate the suitability of Pt/TiWC core–shell materials for ORR applications, we conducted additional long-term durability tests in O_2-sat electrolyte and at elevated temperatures. In situ SFC–ICP–MS experiments measured the dissolution of 2 ML Pt/TiWC over 1,000 cycles between 0.4 and 1.0 V_{RHE} at 1 V s^{-1} in both Ar-sat and O_2-sat 0.1 M $HClO_4$ at either room temperature or 60 °C. Neither the presence of O_2 nor the increase in temperature resulted in a considerable increase in dissolution. For each condition, only around 3% of W and 0.1% of Pt dissolved in total during the 1,000 cycles (Supplementary Fig. 8b), most of which occurred during the first 400 cycles, probably due to the presence of core–shell particles with incomplete Pt coverage (Fig. 3a). Following this initial period, minimal dissolution occurred with 0.1% or less of W and undetectable amounts of Pt dissolving in total over the last 100 cycles. These results suggest that homogeneously coated 2 ML Pt/TiWC particles are completely stable in O_2-sat electrolyte at elevated temperatures. This was further confirmed by STEM–EDX, which showed preservation of the core–shell structure after the AST consisting of 10,800 cycles between 0.4 and 1.0 V_{RHE} in O_2-sat 0.1 M $HClO_4$ at 60 °C (Fig. 3b).

The durability of 2 ML Pt/TiWC as an ORR catalyst was further evaluated by comparing its activity and electrochemical surface area (ECSA) before and after 10,800 cycles in O_2-sat electrolyte to those of a commercial Pt/C catalyst (TKK, 46 wt%, 3 nm) (Fig. 4). The ORR activity was obtained via thin film rotating disc electrode (RDE) measurements at 1,600 r.p.m. in O_2-sat 0.1 M $HClO_4$ and the Pt ECSA was measured from CO stripping (Supplementary Figs. 11 and 12). Initially, 2 ML Pt/TiWC displayed an enhanced specific activity of 0.69 mA cm^{-2}_{Pt} over Pt/C (0.47 mA cm^{-2}_{Pt}), which may be attributed to a weaker oxygen binding energy[27] resulting from its slightly downshifted Pt d-band centre relative to pure Pt[28]. After the AST with O_2, the Pt/C control showed a 19% loss in ECSA, 36% loss in mass activity and 22% loss in specific activity, similar to previous work by Hasché et al.[29]. In contrast, 2 ML Pt/TiWC showed only a 9% loss in ECSA, 22% loss in mass activity and 14% loss in specific activity. For Pt/C, multiple mechanisms have been reported to contribute to the sizeable decrease in ECSA after cycling, including agglomeration, Ostwald ripening, dissolution and particle detachment[13,30]. For 2 ML Pt/TiWC, the losses in performance can all be linked to the corrosion of imperfect core–shell particles, as other degradation mechanisms were not observed in the IL–STEM–EDX or in situ SFC–ICP–MS experiments. When these imperfect

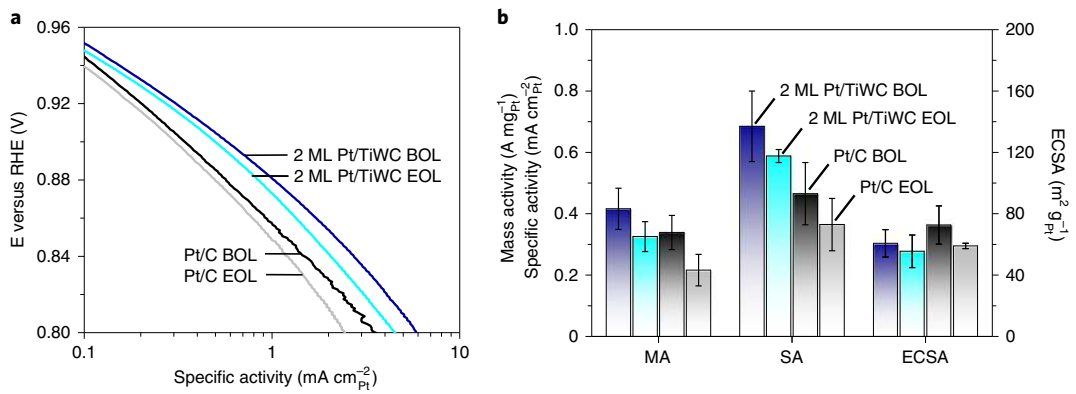

Fig. 4 | ORR catalytic stability. a, Tafel plots normalized to ECSA before (BOL) and after (EOL) ASTs consisting of 10,800 cycles between 0.4 and 1.0 V_{RHE} in O_2-sat 0.1 M $HClO_4$ at a scan rate of 1 V s^{-1}. **b**, Mass activity (MA) at 0.9 V_{RHE}, specific activity (SA) at 0.9 V_{RHE}, and ECSA from CO stripping before and after ASTs in O_2-sat 0.1 M $HClO_4$. Activity was determined from background and iR-corrected ORR polarization curves in O_2-sat 0.1 M $HClO_4$ at 50 mV s^{-1} and 1,600 r.p.m. with Pt loading of 5 μg_{Pt} cm^{-2} for 2 ML Pt/TiWC and 20 μg_{Pt} cm^{-2} for Pt/C (TKK, 46 wt%). Error bars represent s.d. of at least three independent measurements.

particles restructured and collapsed, the ECSA decreased slightly from the loss of Pt surface sites into the bulk of the newly formed Pt NPs, while the specific activity dropped more substantially due to the lower activity of Pt NPs compared to 2 ML Pt/TiWC. Thus, further optimization of the synthesis method to produce more uniform core–shell particles should result in even greater improvement in performance. Evidently, these results demonstrate the enhanced catalytic stability of the core–shell material over traditional monometallic Pt/C catalysts.

In summary, we have shown how nanostructured core–shell materials with TMC or TMN cores can be engineered to have high stability in harsh, oxidative electrochemical environments. SFC–ICP–MS and IL–STEM–EDX experiments revealed the ability of atomically thin Pt shells to protect the TiWC and TiWN cores against dissolution while emphasizing the need for complete, uniform shell coverage. Notably, 2 ML Pt/TiWC NPs with a homogeneous Pt coating exhibited no degradation in the core–shell structure or atomic composition during ASTs with over 10,000 potential cycles in O_2-sat electrolyte at elevated temperatures. This unique performance, including the absence of leaching, alloying and agglomeration, arises specifically from the stabilizing interaction between the noble metal shell and the TMC core. In addition, the increased catalytic durability compared to Pt/C for ORR highlights potential industrial applications. These results provide a detailed insight into the underlying degradation mechanisms that affect the stability of core–shell nanomaterials and also illustrate promising design strategies using earth-abundant TMC and TMN cores to develop low-cost, ultradurable core–shell catalysts.

Online content

Any methods, additional references, Nature Research reporting summaries, source data, extended data, supplementary information, acknowledgements, peer review information; details of author contributions and competing interests; and statements of data and code availability are available at https://doi.org/10.1038/s41563-019-0555-5.

Received: 19 August 2018; Accepted: 7 November 2019;
Published online: 16 December 2019

References

1. Strasser, P. et al. Lattice-strain control of the activity in dealloyed core–shell fuel cell catalysts. *Nat. Chem.* **2**, 454–460 (2010).
2. Gasteiger, H. A. & Marković, N. M. Just a dream—or future reality? *Science* **324**, 48–49 (2009).
3. Stephens, I. E. L., Bondarenko, A. S., Grønbjerg, U., Rossmeisl, J. & Chorkendorff, I. Understanding the electrocatalysis of oxygen reduction on platinum and its alloys. *Energy Environ. Sci.* **5**, 6744–6762 (2012).
4. Oezaslan, M., Hasché, F. & Strasser, P. Pt-Based core–shell catalyst architectures for oxygen fuel cell electrodes. *J. Phys. Chem. Lett.* **4**, 3273–3291 (2013).
5. Wang, X. et al. Palladium-platinum core–shell icosahedra with substantially enhanced activity and durability towards oxygen reduction. *Nat. Commun.* **6**, 7594 (2015).
6. Schwammlein, J. N. et al. Origin of superior activity of Ru@Pt core–shell nanoparticles towards hydrogen oxidation in alkaline media. *ECS Trans.* **75**, 971–982 (2016).
7. Alayoglu, S., Nilekar, A. U., Mavrikakis, M. & Eichhorn, B. Ru-Pt core–shell nanoparticles for preferential oxidation of carbon monoxide in hydrogen. *Nat. Mater.* **7**, 333–338 (2008).
8. Sasaki, K. et al. Core-protected platinum monolayer shell high-stability electrocatalysts for fuel-cell cathodes. *Angew. Chem. Int. Ed.* **49**, 8602–8607 (2010).
9. Tedsree, K. et al. Hydrogen production from formic acid decomposition at room temperature using a Ag-Pd core–shell nanocatalyst. *Nat. Nanotech* **6**, 302–307 (2011).
10. Strickler, A. L., Jackson, A. & Jaramillo, T. F. Active and stable Ir@Pt core–shell catalysts for electrochemical oxygen reduction. *ACS Energy Lett.* **2**, 244–249 (2016).
11. Cui, C., Gan, L., Heggen, M., Rudi, S. & Strasser, P. Compositional segregation in shaped Pt alloy nanoparticles and their structural behaviour during electrocatalysis. *Nat. Mater.* **12**, 765–771 (2013).
12. Chen, S., Gasteiger, H. A., Hayakawa, K., Tada, T. & Shao-Horn, Y. Platinum-alloy cathode catalyst degradation in proton exchange membrane fuel cells: nanometer-scale compositional and morphological changes. *J. Electrochem. Soc.* **157**, A82–A97 (2010).
13. Perez-Alonso, F. J. et al. Identical locations transmission electron microscopy study of Pt/C electrocatalyst degradation during oxygen reduction reaction. *J. Power Sources* **196**, 6085–6091 (2011).
14. Knossalla, J. et al. Shape-controlled nanoparticles in pore-confined space. *J. Am. Chem. Soc.* **140**, 15684–15689 (2018).
15. Hunt, S. T. et al. Self-assembly of noble metal monolayers on transition metal carbide nanoparticle catalysts. *Science* **352**, 974–978 (2016).
16. Zhong, Y. et al. Transition metal carbides and nitrides in energy storage and conversion. *Adv. Sci.* **3**, 1500286 (2016).
17. Hunt, S. T., Nimmanwudipong, T. & Roman-Leshkov, Y. Engineering non-sintered, metal-terminated tungsten carbide nanoparticles for catalysis. *Angew. Chem.* **53**, 5131–5136 (2014).
18. Kuttiyiel, K. A. et al. Enhancement of the oxygen reduction on nitride stabilized Pt-M (M=Fe, Co, and Ni) core–shell nanoparticle electrocatalysts. *Nano Energy* **13**, 442–449 (2015).
19. Tian, X. et al. Transition metal nitride coated with atomic layers of Pt as a low-cost, highly stable electrocatalyst for the oxygen reduction reaction. *J. Am. Chem. Soc.* **138**, 1575–1583 (2016).
20. Garg, A. et al. Transition-Metal nitride Core@Noble-Metal shell nanoparticles as highly CO tolerant catalysts. *Angew. Chem. Int. Ed.* **56**, 8828–8833 (2017).
21. Hunt, S. T., Milina, M., Wang, Z. & Roman-Leshkov, Y. Activating earth-abundant electrocatalysts for efficient, low-cost hydrogen evolution/oxidation: sub-monolayer platinum coatings on titanium tungsten carbide nanoparticles. *Energy Environ. Sci.* **9**, 3290–3301 (2016).
22. Garg, A. *Transition Metal Carbide and Nitride Nanoparticles with Noble Metal Shells as Enhanced Catalysts* (Massachusetts Institute of Technology, 2018).
23. Topalov, A. A. et al. Dissolution of platinum: limits for the deployment of electrochemical energy conversion? *Angew. Chem.* **51**, 12613–12615 (2012).
24. Göhl, D. et al. Electrochemical stability of hexagonal tungsten carbide in the potential window of fuel cells and water electrolyzers investigated in a half-cell configuration. *Electrochim. Acta* **270**, 70–76 (2018).
25. Weidman, M. C., Esposito, D. V., Hsu, I. J. & Chen, J. G. Electrochemical stability of tungsten and tungsten monocarbide (WC) over wide ph and potential ranges. *J. Electrochem. Soc.* **157**, F179–F188 (2010).
26. Pourbaix, M. *Atlas of Electrochemical Equilibria in Aqueous Solutions* (National Association of Corrosion Engineers, 1974).
27. Greeley, J. et al. Alloys of platinum and early transition metals as oxygen reduction electrocatalysts. *Nat. Chem.* **1**, 552–556 (2009).
28. Hendon, C. H. et al. Realistic surface descriptions of heterometallic interfaces: the case of TiWC coated in noble metals. *J. Phys. Chem. Lett.* **7**, 4475–4482 (2016).
29. Hasche, F., Oezaslan, M. & Strasser, P. Activity, stability and degradation of multi walled carbon nanotube (MWCNT) supported Pt fuel cell electrocatalysts. *Phys. Chem. Chem. Phys.* **12**, 15251–15258 (2010).
30. Meier, J. C. et al. Design criteria for stable Pt/C fuel cell catalysts. *Beilstein J. Nanotechnol.* **5**, 44–67 (2014).

Methods

Materials synthesis. Silica encapsulated titanium tungsten oxide NPs coated with a desired amount of Pt salt (denoted as $SiO_2/(NH_4)_2PtCl_6$/TiWO) were synthesized using a reverse microemulsion (RME) method by first mixing *n*-heptane, Brij-L4 surfactant, ultrapure water (18 MΩ cm^{-1}), NH_4OH solution, tungsten isopropoxide and titanium isopropoxide. The mixture was stirred for 4 h to allow the $Ti_{0.1}W_{0.9}O_x$ NPs to form. Afterwards, a separate RME containing *n*-heptane, Brij-L4 and chloroplatinic acid dissolved in water was added dropwise to the first RME causing the precipitation of the Pt salt onto the TiWO NPs. After another 4 h, tetraethyl orthosilicate was added and left to react for 16.5 h, encapsulating the particles in a SiO_2 shell. Then, methanol was added to precipitate the $SiO_2/(NH_4)_2PtCl_6$/TiWO NPs, which were recovered after centrifugation and washing with acetone. SiO_2/Pt/TiWC core–shell particles were formed by heating the oxide powder up to 900 °C at a ramp rate of 2 °C min^{-1} under a gas flow of 15% CH_4–85% H_2 and held for 5 h. After cooling to room temperature under H_2, the samples were passivated using 1% O_2–99% N_2 flow. The SiO_2 was removed by dissolution in a mixture of degassed ethanol and aqueous HF solution for 18 h at room temperature with dispersed carbon black added as a support. The carbon-supported Pt/TiWC NPs were recovered through centrifugation, washed thoroughly with degassed ethanol and water, and dried under vacuum. To synthesize Pt/TiWN, the Pt/TiWC powder was heated up to 800 °C at a ramp rate of 2 °C min^{-1} under NH_3 flow and held for 3 h. After cooling to room temperature under NH_3, the samples were passivated. Complete synthetic details are provided in ref. [20].

Pt NPs were synthesized via the ethylene glycol route described in literature. Here, 3.13 ml of a H_2PtCl_6 solution in water (8 wt%, Sigma-Aldrich) were dissolved in 22 ml of ethylene glycol and mixed with 25 ml of a 0.5 M NaOH solution in ethylene glycol. The mixture was heated up to 150 °C while stirring and held there for 1.5 h after its colour turned from orange to brownish black. After the completion of the reaction, 3 ml of a 1 M HCl solution were added to precipitate the NPs, which were recovered through centrifugation and washing with 1 M HCl. Once dried, the Pt NPs were dispersed in acetone along with WC particles (d = 190 nm, Sigma-Aldrich) via ultrasonication while evaporating the solvent. The deposition on WC was confirmed via TEM imageing on a JEOL JEM 2200FS operating at 200 kV. For the SFC measurements, Pt NPs/bulk WC was re-dispersed in water and deposited on a glassy carbon plate with a total loading of 1 and 0.25 µg of W and Pt, respectively. The dissolution was measured during a potential cycle sequence at 2 mV s^{-1} consisting of two cycles up to 0.5 V_{RHE} followed by one cycle up to 1.5 V_{RHE} and ending with one more cycle up to 0.5 V_{RHE}.

Characterization. Powder X-ray diffraction was performed on a Bruker D8 diffractometer using Cu Kα radiation with a step size of 0.02° and step time of 0.2 s. TEM was performed on a JEOL 2010F equipped with a field emission gun operating at 200 kV. Sample elemental composition was measured on an Agilent 7900 ICP–MS. IL–STEM was performed on a FEI Titan 80–200 (ChemiSTEM) with a C_s-corrector (CEOS GmbH) and a high angle annular dark field detector. The microscope was operated at 80 kV to minimize beam damage. 'Z-contrast' conditions were achieved using a probe semi-convergence angle of 24.7 mrad and an inner collection semi-angle of 88.4 mrad. Elemental maps were recorded by EDX using four large solid angle symmetrical Si drift detectors. For the quantification, Pt L, W L and Ti K-edges were used.

SFC–ICP–MS measurements. Here, 0.7 µl of aqueous catalyst suspension was drop-casted onto a polished glassy carbon plate and enclosed by the opening of the SFC. The loading for Pt and W on the glassy carbon plate was 0.03 and 0.15 µg per spot, respectively. A Ag/AgCl reference electrode was placed behind the outlet of the SFC and was calibrated against a RHE before each measurement. A graphite rod counter electrode was placed before the inlet. The 0.1 M $HClO_4$ electrolyte was stored in a small reservoir where it was purged with Ar or O_2 and then pumped at a constant flow rate of 380 µl min^{-1} through the SFC and into the ICP–MS (Perkin Elmer NexION 350X). Although the electrolyte was initially purged with Ar, slight O_2 intrusion could not be avoided resulting in a dilute O_2 concentration about 100 times less than the saturation limit. After the electrolyte left the SFC, it was mixed via a V-connector with an internal standard containing 10 µg l^{-1} Re and Sc and then introduced into the ICP–MS. The Sc^{45}, Ti^{47}, W^{184}, Re^{187} and Pt^{195} isotopes were used to measure the concentration in the electrolyte. The delay time of 17 s between dissolution at the working electrode and detection at the ICP–MS was compensated by calibrating the time scale. The current density and the concentration of dissolved metals were normalized to the ECSA. For samples containing Pt, the value obtained from CO stripping during RDE tests was used. For samples without Pt, the ECSA was estimated assuming an average particle size of 5 nm. Complete details on the SFC–ICP–MS setup are provided in ref. [31].

For the single potential cycle experiments, samples were pretreated with 0.5 M NaOH and rinsed with ultrapure water to reduce the amount of surface oxides and improve the resolution of the experiment. Then, a slow CV scan at 2 mV s^{-1} from 0.0 to 1.5 V_{RHE} was conducted. All potentials are reported versus the RHE. For the galvanostatic experiments, there was no NaOH pretreatment to allow for quantitative comparison of the overall amount of dissolved metal. These experiments began with two reductive cycles, followed by two oxidative, one reductive and finally one oxidative cycle. Each cycle consisted of a 3 min period at open circuit voltage followed by a 3 min period at a current density of ±0.1 mA cm$^{-2}_{ECSA}$ according to whether it was a reductive or oxidative cycle. For the long-term durability experiments, the dissolution was measured during an AST consisting of 1,000 cycles from 0.4 to 1.0 V_{RHE} at 1 V s^{-1} in Ar or O_2-sat 0.1 M $HClO_4$ at room temperature or 60 °C.

IL–STEM measurements. Here, 10 µl of an aqueous catalyst suspension (0.05 g_{cat} l^{-1}) was drop-casted on a gold TEM finder grid (S147A9, Plano GmbH) and dried. After acquiring several high angle annular dark field STEM images of different regions and the corresponding elemental maps, the catalyst-coated TEM grid was used as a working electrode for the AST consisting of 10,800 cycles between 0.4 and 1.0 V_{RHE} at 1 V s^{-1} in Ar-sat or O_2-sat 0.1 M $HClO_4$ at room temperature or 60 °C. A Gaskatel HydroFlex RHE was used as the reference electrode and a graphite rod as the counter electrode. The potential was controlled by a Bio-Logic Science Instruments SP-50 potentiostat. The ohmic potential drop (iR drop) was measured by the current interrupt method and corrected for. After the AST, the grid was rinsed with ultrapure water to remove electrolyte residues and dried. The grid was then re-analysed at identical locations.

RDE measurements. The measurements were performed at room temperature on a Gamry Reference 600 potentiostat with an in-house developed RDE setup. Before measurements, the iR drop in the cell was determined by high frequency impedance. A three-compartment Teflon cell was used with a graphite rod counter electrode and Ag/AgCl reference electrode separated by a Nafion membrane (Tschurl modification) to avoid chloride contamination. The reference electrode was calibrated against a RHE before each measurement and all potentials are reported versus RHE. Catalyst suspensions were prepared by sonicating the samples in 1 ml ultrapure water (Elga PURELAB Plus, 18 MΩ cm^{-1}, TOC < 3 ppb) for 30 min with the concentration of Pt and W as 0.05 and 0.1 g l^{-1}, respectively. Then, 20 µl of this suspension was loaded onto a polished 5 mm GC RDE tip and then dried to form the working electrode. The Pt loading was 5 μg_{Pt} cm$^{-2}_{geo}$ for 2 ML Pt/TiWC and 20 μg_{Pt} cm$^{-2}_{geo}$ for Pt/C (TKK, 46 wt%). The 0.1 M $HClO_4$ electrolyte was prepared from ultrapure water and 70% $HClO_4$ (Merck Suprapur).

The catalyst surface was first pretreated in Ar-sat electrolyte with 20 CV conditioning scans from 0.05 to 1.0 V_{RHE} at 200 mV s^{-1}. Afterwards, ORR polarization curves were recorded in O_2-sat electrolyte at 50 mV s^{-1} and 1,600 r.p.m. with iR compensation. A background was recorded in Ar-sat electrolyte using identical conditions and subtracted to obtain the ORR current. CO stripping and hydrogen underpotential deposition (H_{upd}) measurements were performed to calculate ECSA values using a conversion factor of 390 and 195 µC cm$^{-2}_{Pt}$, respectively, according to ref. [32]. A CV at 50 mV s^{-1} and 0 r.p.m. was recorded to calculate the H_{upd} ECSA, which was done after subtracting the background in CO-sat electrolyte. To obtain the CO stripping voltammograms, the electrode was held at 0.05 V_{RHE} as the electrolyte was purged with CO for 7 min to saturate the surface and then with Ar for 25 min to remove excess CO. Immediately after, a CV was recorded from 0.05 to 1.0 V_{RHE} at 50 mV s^{-1}. CO stripping did not lead to enhanced degradation or restructuring (Supplementary Fig. 9), and the values obtained by the two methods were very similar (Supplementary Fig. 11). The catalytic stability was evaluated using an AST protocol consisting of 10,800 cycles between 0.4 and 1.0 V_{RHE} at 1 V s^{-1} in O_2-sat 0.1 M $HClO_4$ at room temperature.

Data availability

Experimental data are available from the corresponding authors on reasonable request.

References

31. Grote, J.-P., Zeradjanin, A. R., Cherevko, S. & Mayrhofer, K. J. J. Coupling of a scanning flow cell with online electrochemical mass spectrometry for screening of reaction selectivity. *Rev. Sci. Instrum.* **85**, 104101 (2014).
32. Mayrhofer, K. J. J. et al. Measurement of oxygen reduction activities via the rotating disc electrode method: from Pt model surfaces to carbon-supported high surface area catalysts. *Electrochim. Acta* **53**, 3181–3188 (2008).

Acknowledgements

This research was funded by the Federal Ministry for Economic Affairs and Energy (BMWi) of Germany in the framework of PtTM@HGS (project number 03ET6080A) and by the Toyota Research Institute through the Accelerated Materials Design and Discovery program. We acknowledge Z. Wang for his help in synthesis of materials, A. Mingers for her help at the ICP–MS and G. Fortunato for the TEM images of Pt NPs/bulk WC.

Author contributions

D.G., A.G., Y.R.-L. and M.L. conceived this study. A.G. synthesized the materials and performed physicochemical characterization. D.G. conducted the electrochemical stability measurements via SFC–ICP–MS. P.P. carried out IL–STEM measurements accompanied with EDX elemental mapping. D.G. and A.G. conducted ORR activity

measurements via RDE. The manuscript was written by A.G., Y.R.-L., D.G. and M.L. All authors discussed the manuscript and the results.

Competing interests
The authors declare no competing interests.

Additional information
Supplementary information is available for this paper at https://doi.org/10.1038/s41563-019-0555-5.

Correspondence and requests for materials should be addressed to Y.R.-L. or M.L.